In Situ Atomic-Scale Study on the Ultralarge Bending Behaviors of TiO_2-B/Anatase Dual-Phase Nanowires

Qiong Liu,[a] Haifei Zhan,[a] Huaiyong Zhu,[a] Hongwei Liu,[b] Ziqi Sun,[a] John Bell[a], Arixin Bo[a] and Yuantong Gu[a]**

[a]School of Chemistry, Physics and Mechanical Engineering, Queensland University of Technology, GPO Box 2434, 4001, Brisbane, QLD, Australia.

[b]Australian Centre for Microscopy and Microanalysis and School of Aerospace, Mechanical & Mechatronic Engineering, The University of Sydney, Sydney, NSW 2006, Australia

Abstract

It is challenging but important to understand the mechanical properties of one-dimensional (1D) nanomaterials for their design and integration into nanodevices. Generally, brittle ceramic nanowires (NWs) cannot withstand a large bending strain. Herein, *in situ* bending deformation of titanium dioxide (TiO_2) NWs with a bronze/anatase dual-phase was carried out inside a transmission electron microscopy (TEM) system. An ultralarge bending strain up to 20.3% was observed on individual NWs. Through an *in situ* atomic-scale study, the large bending behavior for a dual-phase TiO_2 NW was found to be related to a continuous crystalline-structure evolution including phase transition, small deformation twinning, and dislocation nucleation and movements. Additionally, no amorphization or crack occurred in the dual-phase TiO_2 NW even under an ultralarge bending strain. These results revealed that an individual ceramic NW can undergo a large bending strain with rich defect activities.

Keywords: dual-phase TiO_2 nanowire, ultralarge bending strain, atomic-scale, defect motion, phase transition

Introduction

Due to the large surface-to-volume ratio of the 1D geometry, semiconductor NWs have received intensive attention in the fields of nanomaterials and nanotechnology in recent years. Their promising applications include nanoelectronics,[1] photovoltaics,[2] and electromechanical devices.[3] While the chemical, photonic and optoelectronic properties of semiconductor NWs have been well investigated, it is also essential to fully understand their mechanical properties, especially for the design and integration of these materials in nanodevices. This consideration is particularly crucial for single-NW-based electronics since the NWs are likely to be subjected to mechanical loading during the integration and working processes.[4,5] It was also found that electric and optoelectronic properties of certain semiconductor NWs can be tuned by changing the Fermi energy level by incorporating a mechanical strain, as has been reported in electromechanical systems,[6-8] further illustrating the importance of the mechanical behaviors. So far, it has been widely reported for semiconductor NWs that they usually exhibit better flexibility than their bulk counterparts. Large elastic mechanical strain and even plasticity at room temperature were reported for various semiconductors NWs such as Si,[9-11] GaAs,[12] and Ge[13] NWs. However, it is still hard to confirm that they all exhibit considerable ductility such as a large bending deformation, due to the covalent bonding in semiconductors (the Peierls force).[13,14] Under a mechanical strain, the large Peierls potential is most likely to drive the propagation of defects, causing crack formation or amorphization in the semiconductor NW.

Among various semiconductors, TiO_2 was found to be environmentally friendly, cost-effective, and chemically stable.[15] Since the first demonstration of photoelectrochemical response in TiO_2 in 1972,[16] this material has been studied extensively. In particular, TiO_2 NWs have superior optoelectronic properties, which has been attributed to the fast electron transport and effective charge transfer in the 1D geometrical channel, making them promising building blocks in nanodevice applications.[4,15,17,18] Previous works also showed that the bandgap of TiO_2 can be altered by applying mechanical strain.[19,20] Even though experimental investigations regarding the mechanical properties of TiO_2 NW have studied the elastic modulus and strength,[21] atomic-scale experimental studies that reveal the mechanical behaviors have been rather limited. The atomic-level understanding on the TiO_2 NW structural evolution under mechanical stress has relied on computational investigations such as molecular dynamics simulations.[22] The lack of direct observation and understanding of the mechanical behaviors of TiO_2 NWs may hinder the applications of these materials. Therefore, in addition to the well-

investigated photonic and optoelectronic properties, more attention should be paid to the mechanical properties of TiO_2 NWs, especially from an experimental atomic-level perspective.

To the best of our knowledge, direct experimental observation on the structural evolution of TiO_2 NWs during bending deformation is still lacking, mainly due to the challenges involved in carrying out the nanoscale bending tests. During the last twenty years, different kinds of techniques have been developed to investigate the mechanical properties of nanostructured materials,[23] for example, using a microelectromechanical system (MEMS) device or a bimetallic-strip device as the testing stage or using an atomic force microscopy (AFM) probe as the manipulator inside a scanning electron microscopy (SEM) or TEM system.[10,12,24,25] Herein, we study the bending behaviors of TiO_2 NWs with an *in situ* TEM bending method using a colloidal film.[9] The advantage of this method is that it can protect the NWs from potential damage and contamination that would be caused by other methods such as focused ion beam that involve the welding of materials.[23] This approach also allows high-resolution real-time observation of the structural evolution. The TiO_2 NWs in this work were characterized as having a unique bronze (TiO_2-B) and anatase dual-phase structure, where small anatase areas are surrounded by the bronze structure. For the first time, an ultralarge bending strain of approximately 20.3% was observed on an individual TiO_2-B/anatase dual-phase NW. Detailed atomic-scale information showed that the bending process was accompanied by the phase transition from TiO_2 anatase to bronze and rich defect activities in the NWs.

Experimental Section

Preparation of TiO_2-B/anatase dual-phase NWs

The dual-phase TiO_2 NWs were synthesized by a facile hydrothermal method,[26] followed by a protonation reaction and an annealing process. Typically, a piece of Ti foil (1.0 × 1.5 cm^2) was cleaned by ultrasonication successively in acetone, ethanol, and deionized water for 20 min each. Then, the foil was placed in a 120 mL Teflon-lined autoclave containing 60 mL of 1 M NaOH. The autoclave was sealed and kept in an oven at 220 °C for 20 h. After the autoclave cooled to room temperature, the Ti foil with $Na_2Ti_2O_4(OH)_2$ (NTO) NWs was rinsed with deionized water and then was immersed in 50 mL of 0.5 M HCl for 30 min to exchange the Na^+ ions with H^+. The obtained Ti foil with $H_2Ti_2O_4(OH)_2$ (HTO) NWs was rinsed with deionized water, dried at 80 °C for 24 h, and calcined at 450 °C for 2 h in the atmosphere.

Sample characterization

A field-emission SEM system (JEOL JSM-7001F, Japan) was used to characterize the morphologies of the samples. X-ray diffraction (XRD) patterns were collected using a Philips PANalytical X'pert pro diffractometer equipped with a graphite monochromator with 40 kV Cu Kα radiation. The crystal structure was further analyzed by TEM (JEOL 2100, Japan).

In situ TEM bending tests

In situ bending tests were carried out inside the TEM using a TEM copper grid with a colloidal thin film.[27] Briefly, TiO_2 NWs were scattered on the pre-broken colloidal film attached on a TEM copper grid. Some NWs may bridge near the cracks of the colloidal film. Irradiated by the electron beam in the TEM, the thin colloidal film was most likely to shrink and bend the NWs that were bridged near the cracks.

Results and Discussion

Structural characterization

The XRD patterns of the samples are compared in Figure 1a. It is observed that the XRD pattern of NTO is nearly the same as that of HTO (JCPDS, 47-0124).[28] For TiO_2, the diffraction peaks at approximately 25°, 27.3°, and 48° index well with the (110), (11$\bar{1}$), and (020) planes of TiO_2-B, respectively.[29] In addition to the peak at 55°, which is the reflection of the (211) planes of anatase TiO_2, the two peaks at approximately 25° and 48° can also be attributed to the (101) and (200) anatase planes.[30] The asymmetry of these two peaks also indicates that the crystal phase is not pure bronze or anatase because the (110) and (020) diffraction peaks of TiO_2-B are very close to the (101) and (200) peaks, respectively, of the anatase phase.[29] The magnified two peaks at approximately 25° and 48° are fitted and shown in Figures 1b and 1c, respectively. The peaks located at 24.9° and 25.3° can be assigned to the (110) planes of TiO_2-B and the (101) planes of anatase TiO_2, respectively (Figure 1b), while the peaks located at 48.4° and 48.05° correspond well to the (020) planes of TiO_2-B and the (200) planes of anatase, respectively (Figure 1c).[29]

Figures 1d shows the top-view SEM image of the TiO_2 NWs. The mean length of the synthesized NWs is found to be greater than 10 μm with the diameters of the NWs ranging from 20 to 80 nm. Figure 1e displays a low-magnification TEM image of a NW with a diameter of ~40 nm and a length of more than 1.4 μm (inset in Figure 1e). The corresponding HRTEM image of the framed area in Figure 1e is shown in Figure 1f, where the *d*-spacings of the marked lattice fringes at the bottom are measured to be 0.36 and 0.58 nm, in good agreement with those

of the $(110)_B$ and $(200)_B$ planes of TiO_2-B, respectively. Meanwhile, another two sets of planes with the *d*-spacings of 0.36 and 0.48 nm can be assigned to the $(0\bar{1}1)_A$ and $(002)_A$ planes of the TiO_2 anatase, respectively. The structural information indicates that $(110)_B$ planes are parallel to the $(0\bar{1}1)_A$ planes with nearly same *d*-spacings and that the $(200)_B$ planes are parallel to the $(002)_A$ planes. This structural feature is also shown by a schematic atomic structure in Figure 1g. The selected area electron diffraction (SAED) pattern (Figure 1h) of the NW shows two sets of diffraction spots, indicating a dual-phase crystalline structure. The SAED pattern is taken along the [001] zone axis for the bronze phase and [100] for the anatase phase. Moreover, it is observed that the diffraction spot of the $(110)_B$ planes is rather close to that of the $(0\bar{1}1)_A$ planes, indicating the two sets of planes are parallel to each other. A SAED model with both TiO_2 bronze and anatase (viewed along [001] for the bronze and [100] for the anatase) is shown in Figure 1i and is consistent with Figure 1h.

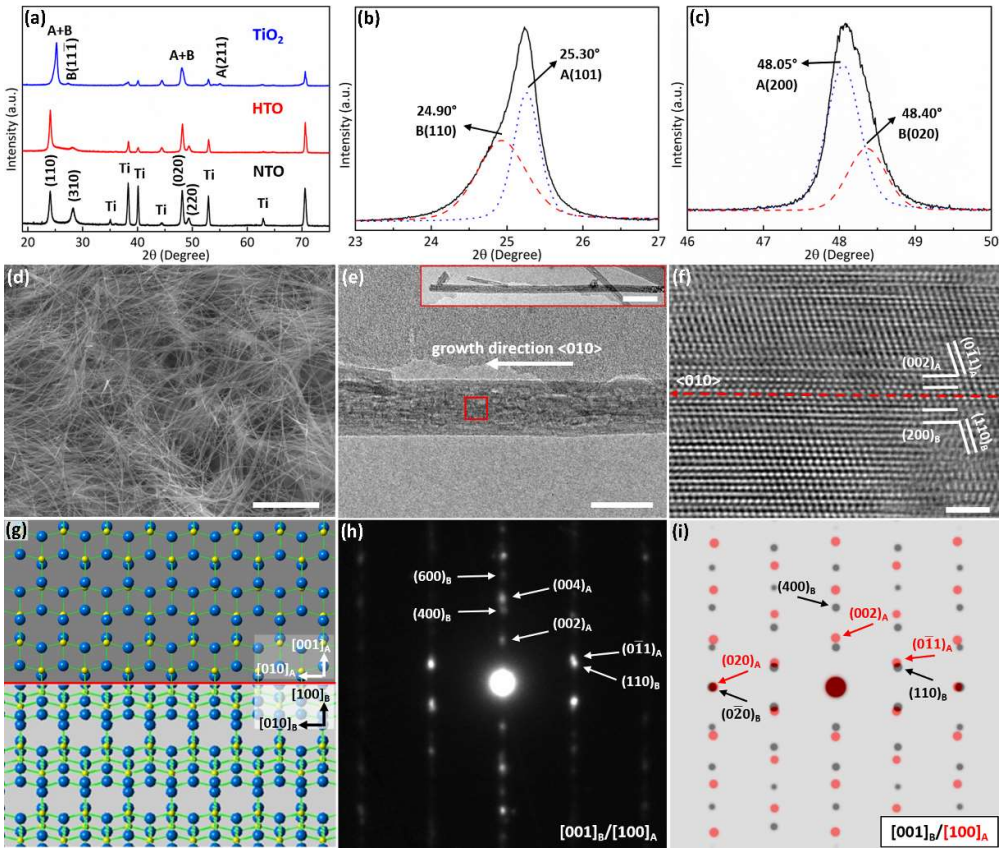

Figure 1. Morphological and crystalline structure characterization of the as-prepared TiO_2 NWs. (a) XRD patterns of $Na_2Ti_2O_4(OH)_2$ (NTO), $H_2Ti_2O_4(OH)_2$ (HTO), and TiO_2 NWs. (b,c) enlarged XRD patterns of TiO_2 at approximately 25° and 48°, respectively. (d) Top-view SEM image of the TiO_2 NW arrays. (e) TEM image, (f) HRTEM image, (g) Schematic crystalline structure, (h) SAED pattern of the TiO_2 NW. (i) SAED model for the TiO_2 with both bronze and anatase phases viewed along $[001]_B$ and $[100]_A$, respectively. The red-dot matrix represents the SAED of anatase TiO_2 and the black-dot matrix represents the SAED of the bronze phase. Scale bar: 3 μm in (d), 50 nm in (e) (200 nm in the inset), 2 nm in (f).

In situ bending tests

In situ bending deformations for the NWs were conducted by shrinking the colloidal thin film under electron beam irradiation inside the vacuum chamber of the TEM.[9] A dynamic bending process of one NW is shown in Movie S1. During the bending process, the electron beam dose rate was maintained at a level of approximately 3×10^{19} e/(cm^2·s) so that the local temperature was only a few degrees higher than the room temperature.[9] Figures 2a-f show a series of TEM images that display the bending process of an individual NW with a diameter of ~44 nm. The bending strain is determined from the curvature of the bent NW, as schematically

illustrated in the upper panel of Figure 2g. The strain ε_x at a distance y from the neutral line of the NW is calculated by the formula, $\varepsilon_x = y/\rho(x)$.[9,13,31] Here, x represents the length direction of the NW, $1/\rho(x)$ is the curvature of the bent NW, y ranges from $-r$ to r (r is the NW radius). As indicated in the TEM images presented in Figures 2d-f, the NW is not under pure bending, *i.e.*, the curvature ρ varies along the long direction of the NW. Since this work focuses on the bending deformation around the region undergoing the largest deformation, the maximum local bending strain (when $y = r$, and $\rho = \rho_{min}$) is adopted to represent the deformation of the NW. For example, in the lower panel of Figure 2g, the maximum bending strain in the local segment of the NW is estimated to be 9.5%. It is observed that the maximum bending strain in the NW increases gradually from 2.5% to an ultralarge value of 20.3%.

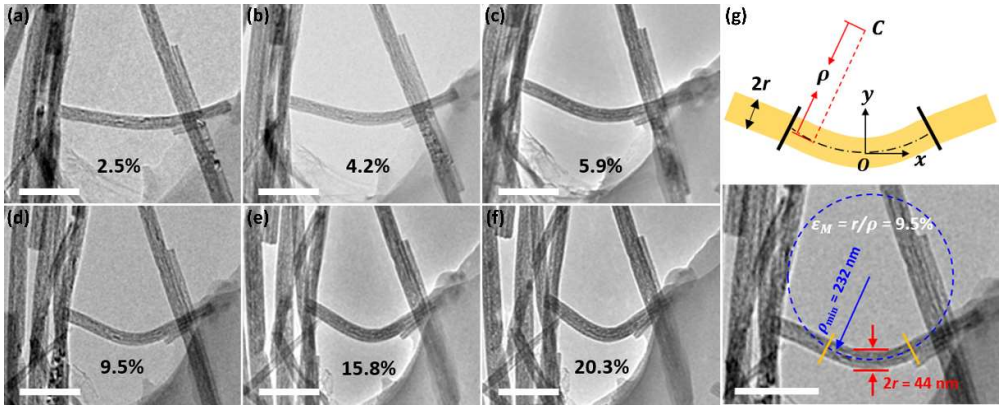

Figure 2. A series of TEM images showing the *in situ* bending process of an individual TiO_2 NW. (a-f) TEM images showing that the bending strain increased from 2.5% to 20.3%. (g) The upper panel is the schematic showing the calculation of the bending strain of a bent NW. The dashed line indicates the ideal neutral-stress line in the NW. The lower panel is an example illustrating the calculation of the maximum bending strain in the NW. Scale bar: 200 nm.

Bending mechanisms

The NW was viewed along $[011]_B$ to precisely distinguish the bronze and anatase phases, from which the structural evolution can be observed more directly during the NW deformation. The viewed orientation was kept constant by double-tilting the NW during bending. Figure 3b shows the HRTEM image of the framed area of the bent NW in Figure 3a with the maximum bending strain of 2.5%. Despite the spots representing the $\{001\}_B$ planes, the encircled spots in the inset FFT pattern cannot be resolved, suggesting the dual-phase structure in the NW. Figure 3c is the enlarged HRTEM image of the framed area in the central region in Figure 3b, showing the existence of both bronze and anatase TiO_2 phases. The

parallelogram area shows the anatase structure with approximately six layers in the $[100]_A$ direction and a width of approximately seventeen $(1\bar{1}\bar{1})_A$ layers. Around the parallelogram area is the TiO_2-B lattice matrix, as is further confirmed by the corresponding FFT pattern (Figure 3d) of the top framed area in Figure 3c. Furthermore, the FFT pattern inside the parallelogram area further confirms the existence of the anatase phase (Figure 3e). The view direction for the NW can be defined both along $[011]_B$ and $[110]_A$.

For a NW under bending deformation, the strain in the NW varies along the radial direction, with the compressive side and the tensile side undergoing a larger compressive strain and tensile strain, respectively. Simultaneously, both sides can have distinct mechanical responses. The strains of the $(11\bar{1})_B$ planes along the lines in the compressive (line-1), central (line-2), and tensile (line-3) regions were measured to illustrate the bending-strain dependence of the lattice strain. The lattice strain of $(11\bar{1})_B$ planes, $\varepsilon_{11\bar{1}}$, is calculated by $\varepsilon_{11\bar{1}} = (d_{11\bar{1}} - d_R)/d_R$,[14,32,33] where d_{11^-} is the *d*-spacing of the $(11\bar{1})_B$ planes measured at a certain position and d_R is the reference value of the $(11\bar{1})_B$ *d*-spacing.[29] As seen in Figure 3f, the $(11\bar{1})_B$ lattice strain along either line-1 or line-3 is larger than that along line-2 (close to the neutral line). This observation further reveals the inhomogeneous strain distribution along the NW radial direction. Curves "1" and "3" show apparent fluctuations, which is probably caused by the generation of dislocations. When the maximum bending strain is increased to 3.5%, the fluctuations of all three curves increase, suggesting a continuous structural evolution in the NW (Figure 3g).

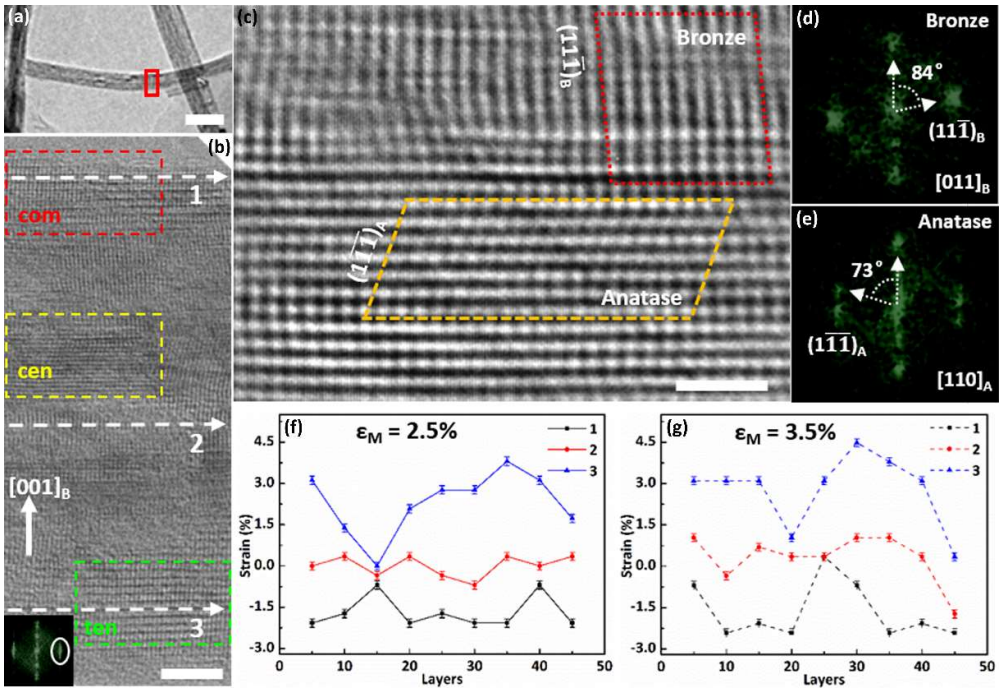

Figure 3. Lattice-structural information of the dual-phase NW with the maximum bending strain increased from 2.5% to 3.5%. (a) TEM image of the NW with a bending strain of 2.5%. (b) HRTEM of the framed area in (a). (c) Enlarged HRTEM image of the central framed area in (b). (d,e) FFT patterns of the framed areas in the top and bottom of (c), respectively. (f,g) $(11\bar{1})_B$ lattice strain distributions along the three lines ("1", "2", and "3") in (b) under the maximum bending strains of 2.5% and 3.5%, respectively. Each dot represents the mean value of every five adjacent layers. Scale bar: 100 nm in (a), 5 nm in (b), 2 nm in (c).

Figures 4a, 4b and 4c show the enlarged HRTEM images of the framed areas located at the compressive ("com"), central ("cen"), and tensile ("ten") regions in Figure 3b under the maximum bending strain of 2.5%, respectively. Figures 4d, 4e and 4f show the enlarged HRTEM images of the same three areas when the bending strain is increased to 3.5%. It is observed from Figures 4a and 4d that the upper-left surface bump increased from three lattice layers to four. Additionally, the dislocation lying in the $(11\bar{1})_B$ planes disappeared from this area while the dislocation lying in the $\{001\}_B$ planes remained stationary. The dislocation movements can also be observed at the tensile side, with the two dislocations lying in the $(11\bar{1})_B$ planes moving away (Figures 4c and 4f). This result suggests that the dislocation movements occurred in both the compressive and tensile sides of the NW. As the bending strain increased, no crack or dislocation propagation was observed. Due to the presence of the dual-phase structure in the central region, the structural evolution becomes more complicated even

though the bending strain in the central region is expected to be smaller than those in the compressive and tensile regions, as indicated in Figures 4b and 4e. Below, we discuss the evolution of the dual-phase structure.

Figures 4g-l show the *in situ* behaviors of the defects and phase transition in the dual-phase structure during the bending deformation at the atomic scale. Figure 4g displays the defect pattern from the image shown in Figure 3c. Two phase-boundaries (PBs) (marked as "1" and "2", respectively) along the $\{001\}_B$ planes are marked by the two arrows at the top and bottom of the anatase area. A number of dislocations (marked by "⊥") lying in the $(11\bar{1})_B$ planes are distributed around the anatase phase, compensating the lattice misfit between the anatase phase and the bronze phase. Two small twinning slabs with their TBs in the $\{001\}_B$ planes and several dislocations lying in the $(11\bar{1})_B$ planes are found below the anatase structure. Figure 4h shows the FFT pattern of the anatase structure where the spots assigned to the $(1\bar{1}\bar{1})_A$ and $\{100\}_A$ planes of the anatase phase are indicated by arrows. Figure 4c shows the lattice information of the same region taken 10 s after Figure 4g. With increasing bending strain, the tetragonal anatase phase was transformed into the monoclinic bronze phase, and the defect pattern was reconfigured. Three strips of lattice planes are marked by the yellow lines, representing the $(11\bar{1})_B$ planes, as indicated by the angle of 84° between the yellow lines and the $\{001\}_B$ planes. The three strips of the $(11\bar{1})_B$ planes are divided by the two original PBs, as shown in Figure 4i. Additionally, the two small twinning slabs and most of the dislocations in the $(11\bar{1})_B$ planes disappeared. The corresponding FFT pattern of Figure 4i is shown in Figure 4j. It can be seen that the diffraction spot representing the $(1\bar{1}\bar{1})_A$ planes cannot be observed, with the appearance of the spot that is assigned to the $(11\bar{1})_B$ planes.

It is known that phase transition can be driven by the lattice shear stress that can be applied on the materials by mechanical deformation or thermal stimulation.[34,35] For instance, Guo *et al.* reported that under compression through grinding with a diamond tip, the diamond cubic (3C) Si transformed to a new tetragonal phase by slips of atoms at a shear stress of 2.16 GPa.[34] In Patriarche's work, Si-3C NWs were found to transform to hexagonal (2H) phase by thermally activated shear stress.[35] Previous works reported that a phase transition occurs in TiO_2 under thermal treatment at a temperature above 500 °C.[36] As the local temperature was close to room temperature during the bending process, the phase transition for the dual-phase TiO_2 NW from anatase to bronze phase should be caused by the mechanical deformation. Planar defects such as stacking faults (SFs), PBs, grain boundaries (GBs), and TBs are

comparative stable defects that can hinder the dislocation motion. Thus, metal or alloys and ceramic nanomaterials can be strengthened by incorporating planar defects into them.[37-39] In other words, under a bending strain, the relatively stable planar defects may confine intense shear stress in small zones (several-nanometer thick) due to the absence of dislocation nucleation and motion.[38] In this case, phase transformation is more likely to occur. For example, nanotwinned Ni NWs can undergo a phase transformation from the face-centered cubic (FCC) lattice to a body-centered tetragonal (BCT) structure, during which an ultralarge reversible lattice shear strain of 34.6% was achieved during the bending deformation.[27] Here, as shown in Figure 4a, the small anatase area (~1.5 nm in thickness) was confined by two PBs, helping inhibit the potential dislocation nucleation and movement. Under the <010>{100} shear, the atoms in the $\{100\}_A$ planes acquire a favorable slip direction along <010>; thus, the small anatase structure confined by the PBs was likely to experience a phase transformation to bronze phase. The phase transition can also be observed in another region, as shown in Figure S1. A small anatase structure in the square box was confined by two PBs (labeled "1" and "2") with the thickness of approximately 6 nm in the $[100]_A$ direction (Figure S1a). The presence of the anatase phase is further confirmed by the corresponding FFT pattern (Figure S1b). When the bending strain is increased to 4.2%, the framed area shows a TiO_2-B feature (Figures S1c and S1d). The two PBs disappeared, leaving a TB lying in the $\{001\}_B$ planes where the PB "1" was located. It should be noted that no large-scale phase transition is triggered under the bending deformation in this work, indicating that it may be difficult for the dual-phase TiO_2 NWs to undergo a large-scale phase transition under a mechanical stress at low temperature. The occurrence of the localized phase transition is attributed to the unique crystalline structure where the anatase structure exists in the form of small slabs in the NWs.

After the strain was further increased, the bronze phase transformed from the anatase structure was well preserved, while the defect pattern continued evolving. A region of the twinning lattice with three TBs appeared (Figure 4k), where TB #1 and TB #2 were derived from the original two PBs "1" and "2" shown in Figure 4g, respectively, indicating the elimination and regeneration of TBs during bending. The FFT pattern (Figure 4l) of this area in Figure 4k shows no difference from that in Figure 4j, suggesting that the TiO_2-B phase remained unchanged. The TB variation during the bending deformation of a TiO_2 NW could also be observed when the NW was viewed along the $[001]_B$ zone axis, as shown in Figure S2. Three TBs lying in the $\{100\}_B$ planes were marked in this region (Figure S2b). After the NW was bent, two TBs ("2" and "3") disappeared with only one ("1") remaining (Figure S2d).

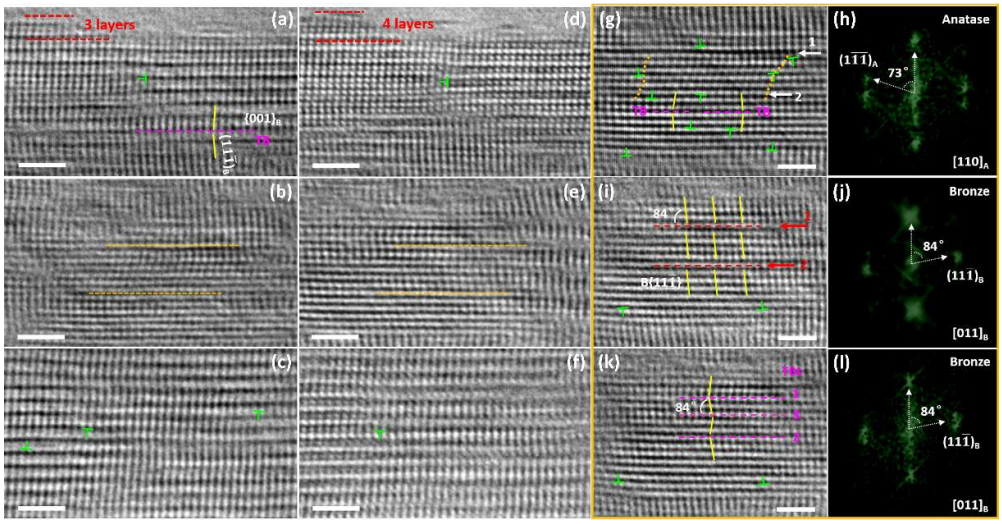

Figure 4. *In situ* atomic-scale observation of the lattice-structural evolution with the bending strain increasing from 2.5% to ~3.5%. (a-c) Enlarged HRTEM images of the framed area located at the compressive ("com"), central ("cen"), and tensile ("ten") regions in Figure 3b, respectively, with the maximum bending strain of 2.5%. (d-f) Enlarged HRTEM images of the same three areas corresponding to (a-c), respectively, but with the maximum bending strain of 3.5%. (g) HRTEM image showing the defect pattern of the dual-phase area with the bending strain of 2.5%. (h) FFT pattern of the anatase structure in (g). (i) HRTEM image taken 10 s after (g) and (j) the corresponding FFT pattern of the same area with (h). (k) HRTEM image taken 30 s after (g) and (l) the corresponding FFT pattern of the same area with (h). Scale bar: 2 nm.

As shown in Figure 5a, the lattice matrix experienced a further structural evolution under a larger bending strain of 4.2%. The TBs around the original anatase area were eliminated, leaving a defect-free bronze structure. The shear strain in the bronze matrix gradually increased, causing a change in the angle between the $(11\bar{1})_B$ and $\{001\}_B$ planes from 84° to 86° and 88° (from left to right). A larger shear strain was most likely impeded by a new nucleated dislocation in the $(11\bar{1})_B$ plane (indicated by the arrow). Additionally, two more new dislocations can be found at the top right and the bottom right in this region. The HRTEM image of the NW under the bending strain of 5.9% is shown in Figure 5b. It is observed that the crystal structure became complex again. First, the $\{001\}_B$ planes were apparently bent with formation of a dislocation lying in the $\{001\}_B$ plane, as indicated by the dashed line. The lattice matrix was under a shear strain along the longitudinal direction of the NW (e.g., <010> for the bronze phase), as indicated by an angle of 76° between the $(11\bar{1})_B$ and $\{001\}_B$ planes of the

bronze phase. Moreover, two small twinning areas were generated, with two dislocations in the $(11\bar{1})_B$ planes heading opposite to each other in between. The two dislocations are also attributed to the large bending strain.

Based on the results discussed above, it is clear that with a continuously increasing bending strain, the dual-phase TiO_2 NW experiences elimination and regeneration of TBs, and dislocation nucleation and slippage occurred in the $(11\bar{1})_B$ planes. The nucleation and disappearance of the dislocations in the $(11\bar{1})_B$ planes suggests that the activities of dislocations in the $(11\bar{1})_B$ planes largely account for the bending strain smaller than 5.9% in this case because the capability for compensating for bending strains by dislocations in the radial planes for a ceramic NW (*i.e.*, $(11\bar{1})_B$ for the TiO_2-B phase) is always limited. For instance, Han *et al.* reported that the bending strain for SiC NWs compensated by a radial dislocation was less than 2%.[40] When a ceramic NW is under a large strain, dislocation propagation, atomic lattice disordering, and ultimately the formation of amorphous regions are usually involved.[9,14] For example, amorphization at the tensile sides of WC NWs was observed when the bending strain was greater than 4%.[14] Wang *et al.* reported that partial dislocations appear in single-crystalline Si NWs with the strain of 6.9% and that lattice disordering was observed when the strain reached 14.3%.[9] As the dislocation in the longitudinal planes ($\{001\}_B$) was formed (Figure 5b), it is assumed that the activities of dislocations in the $\{001\}_B$ planes may further contribute to a bending strain larger than 5.9%. Therefore, a larger bending deformation may better reveal whether or not the activities of the dislocations lying in $\{001\}_B$ planes can lead to an ultralarge bending strain for the dual-phase TiO_2 NWs.

Figure 5 shows the HRTEM image in the framed area of the NW under the bending strain of 9.5% (Figure 5c). Two dislocations in the $\{001\}_B$ planes (marked as #1 and #2) and a PB are observed that separate the anatase lattice matrix (bottom-half part) from the bronze matrix (top-half part). In the TiO_2-B area, a small twinning region is also found. The nucleation of additional dislocations in longitudinal $\{001\}_B$ planes disperses the strain energy when the NW was under a much larger external loading. Figures 5e shows the HRTEM image taken 20 s after that shown in Figure 5d. With increasing bending strain, dislocation #2 disappeared while dislocation #1 remained intact, confirming that the activities of dislocations in the $\{001\}_B$ planes became vigorous. Meanwhile, the TBs in the TiO_2-B matrix were eliminated, indicating that the activity of TBs was still invigorated when the NW was under a very large bending strain.

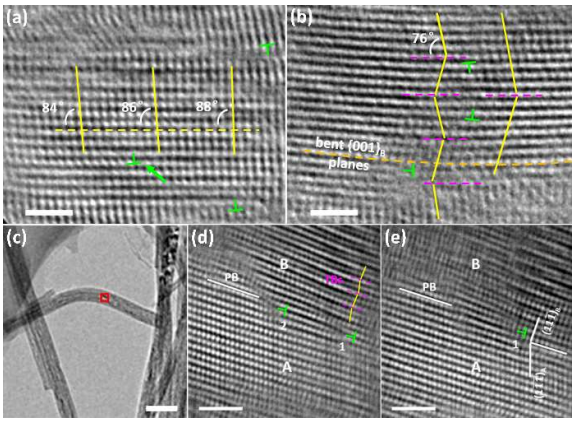

Figure 5. Defect patterns with increasing bending strains. (a,b) HRTEM images corresponding to the same area in Figure 4g, with bending strains of 4.2% and 5.9%, respectively. (c) Low-magnification TEM image of the bent NW with a bending strain of 9.5%. (d,e) HRTEM images of the framed area in (c), taken with a time interval of 20 s. "A" and "B" represent the anatase phase and bronze phase, respectively. Scale bar: 2 nm in (a), (b), (d), and (e), 100 nm in (c).

Generally, a large bending strain for a defect-free metallic NW benefits from its plasticity resulting from dislocation nucleation and the subsequent slippage or deformation twinning.[25] By contrast, the brittleness of ceramic NWs is caused by the dislocations in them that are often sessile and tend to rapidly propagate, ultimately resulting in a crack.[39] Nevertheless, ultralarge bending strain and plasticity have been reported for ceramic NWs. For example, a large bending strain of up to 14% was observed on Si NWs, which was associated with partial and full dislocation nucleation, motion, and lattice disordering.[9] Here, for the dual-phase TiO_2 NWs, the large bending strain involves the phase transition from anatase to bronze, deformation twinning, lattice shearing, and rich dislocation activities. Large bending deformation (strain > 5.9%) can activate the dislocation nucleation in the $\{001\}_B$ planes. Before the bending strain reached 9.5%, no large-scale lattice disorder and amorphization was driven. To validate that lattice disorder and amorphization were still absent under an ultralarge bending strain, the lattice information of the NW under the ultralarge bending strain of 20.3% is displayed in Figure S3. Figures S3a and S3b show the HRTEM images of the compressive and tensile side of the frame area in the inset of Figure S3a, respectively. No obvious lattice disordering and amorphous regions is observed in neither the compressive nor the tensile side. Instead, a large number of dislocations in the $\{001\}_B$ planes nucleated and were distributed randomly. It is believed that the formation of these energy-cost dislocations in the $\{001\}_B$ planes allows the dual-phase TiO_2 NW to withstand large stress without decrystallization,

which is different from the bending behaviors of other ceramic NWs, such as those of SiC and Si.

Conclusion

In summary, for the first time, we investigate the bending behaviors of TiO_2 NWs with a TiO_2-B/anatase dual-phase structure through *in situ* bending tests inside a TEM system. The bending deformation was found to be accompanied by the phase transition, deformation twinning, and rich dislocation nucleation and movements. In particular, due to the unique crystalline structure of the dual-phase TiO_2 where small anatase-phase slabs coexist with the bronze phase, the nanoconfined anatase areas undergo a phase transition from TiO_2 anatase to bronze. Due to the active structural evolution, an ultralarge bending strain of 20.3% for an individual TiO_2 NW was observed with no amorphization or crack in the NW. These results may challenge our knowledge that a large bending deformation on a ceramic NW usually results in amorphization or fracture. This work launches the study on the mechanisms of bending behaviors of TiO_2 NWs and can provide valuable information for the design of TiO_2-NW-based devices.

Supporting Information

Movie of an *in situ* TEM bending test. Atomic-scale observation of the phase transition. More information on TB behaviors. Dislocation patterns of the NW with an ultralarge bending strain.

Acknowledgments

We acknowledge the support from the Australian Research Council (ARC) Discovery Project (DP170102861) and the Central Analytical Research Facility (CARF) of Queensland University of Technology (QUT).

References

1. Ernst, T. *Science* **2013**, *340* (6139), 1414-1415.

2. Krogstrup, P.; Jørgensen, H. I.; Heiss, M.; Demichel, O.; Holm, J. V.; Aagesen, M.; Nygard, J.; i Morral, A. F. *Nat. Photonics* **2013**, *7* (4), 306.

3. Wu, W.; Wang, Z. L. *Nat. Rev. Mater.* **2016**, *1* (7), 16031.

4. Lin, Z.-H.; Xie, Y.; Yang, Y.; Wang, S.; Zhu, G.; Wang, Z. L. *ACS Nano* **2013**, *7* (5), 4554-4560.

5. Luo, W.; Weng, Q.; Long, M.; Wang, P.; Gong, F.; Fang, H.; Luo, M.; Wang, W.; Wang, Z.; Zheng, D. *Nano Lett.* **2018**, *18* (9), 5439-5445.

6. Huang, C.-T.; Song, J.; Lee, W.-F.; Ding, Y.; Gao, Z.; Hao, Y.; Chen, L.-J.; Wang, Z. L. *J. Am. Chem. Soc.* **2010**, *132* (13), 4766-4771.

7. Arcizet, O.; Jacques, V.; Siria, A.; Poncharal, P.; Vincent, P.; Seidelin, S. *Nat. Phys.* **2011**, *7* (11), 879.

8. Johnson, J. C.; Choi, H.-J.; Knutsen, K. P.; Schaller, R. D.; Yang, P.; Saykally, R. J. *Nat. Mater.* **2002**, *1* (2), 106.

9. Wang, L.; Zheng, K.; Zhang, Z.; Han, X. *Nano Lett.* **2011**, *11* (6), 2382-2385.

10. Tang, D.-M.; Ren, C.-L.; Wang, M.-S.; Wei, X.; Kawamoto, N.; Liu, C.; Bando, Y.; Mitome, M.; Fukata, N.; Golberg, D. *Nano Lett.* **2012**, *12* (4), 1898-1904.

11. Stan, G.; Krylyuk, S.; Davydov, A.; Levin, I.; Cook, R. F. *Nano Lett.* **2012**, *12* (5), 2599-2604.

12. Wang, Y. B.; Wang, L. F.; Joyce, H. J.; Gao, Q.; Liao, X. Z.; Mai, Y. W.; Tan, H. H.; Zou, J.; Ringer, S. P.; Gao, H. J. *Adv. Mater.* **2011**, *23* (11), 1356-1360.

13. Smith, D. A.; Holmberg, V. C.; Korgel, B. A. *ACS Nano* **2010**, *4* (4), 2356-2362.

14. Sun, Y.; Chen, Y.; Cui, H.; Wang, J.; Wang, C. *Small* **2017**, *13* (29), 1700389.

15. Ge, M.; Cao, C.; Huang, J.; Li, S.; Chen, Z.; Zhang, K.-Q.; Al-Deyab, S.; Lai, Y. *J. Mater. Chem. A* **2016**, *4* (18), 6772-6801.

16. Fujishima, A.; Honda, K. *Nature* **1972**, *238* (5358), 37.

17. Li, X.; Dai, S.-M.; Zhu, P.; Deng, L.-L.; Xie, S.-Y.; Cui, Q.; Chen, H.; Wang, N.; Lin, H. *ACS Appl. Mater. Inter.* **2016**, *8* (33), 21358-21365.

18. Wang, X.; Li, Z.; Shi, J.; Yu, Y. *Chem. Rev.* **2014**, *114* (19), 9346-9384.

19. Yin, W.-J.; Chen, S.; Yang, J.-H.; Gong, X.-G.; Yan, Y.; Wei, S.-H. *Appl. Phys. Lett.* **2010**, *96* (22), 221901.

20. Benson, E. E.; Miller, E. M.; Nanayakkara, S. U.; Svedruzic, D.; Ferrere, S.; Neale, N. R.; van de Lagemaat, J.; Gregg, B. A. *Chem. Mater.* **2017**, *29* (5), 2173-2179.

21. Zhao, Z.; Tian, J.; Sang, Y.; Cabot, A.; Liu, H. *Adv. Mater.* **2015**, *27* (16), 2557-2582.

22. Dai, L.; Sow, C.; Lim, C.; Cheong, W.; Tan, V. *Nano Lett.* **2009**, *9* (2), 576-582.

23. Wang, S.; Shan, Z.; Huang, H. *Adv. Sci.* **2017**, *4* (4), 1600332.

24. Cheng, G.; Miao, C.; Qin, Q.; Li, J.; Xu, F.; Haftbaradaran, H.; Dickey, E. C.; Gao, H.; Zhu, Y. *Nat. Nanotechnol.* **2015**, *10* (8), 687.

25. Wang, L.; Teng, J.; Sha, X.; Zou, J.; Zhang, Z.; Han, X. *Nano Lett.* **2017**, *17* (8), 4733-4739.

26. Li, K.; Li, B.; Wu, J.; Kang, F.; Kim, J.-K.; Zhang, T.-Y. *ACS Appl. Mater. Inter.* **2017**, *9* (41), 35917-35926.

27. Wang, L.; Liu, P.; Guan, P.; Yang, M.; Sun, J.; Cheng, Y.; Hirata, A.; Zhang, Z.; Ma, E.; Chen, M. *Nat. Commun.* **2013**, *4*, 2413.

28. Que, L.; Wang, Z.; Yu, F.; Gu, D. *J. Mater. Chem. A* **2016**, *4* (22), 8716-8723.

29. Beuvier, T.; Richard-Plouet, M.; Mancini-Le Granvalet, M.; Brousse, T.; Crosnier, O.; Brohan, L. *Inorg. Chem.* **2010**, *49* (18), 8457-8464.

30. Liao, J.-Y.; Higgins, D.; Lui, G.; Chabot, V.; Xiao, X.; Chen, Z. *Nano Lett.* **2013**, *13* (11), 5467-5473.

31. Landau, L. D.; Lifshitz, E.M. *Theory of Elasticity* (Pergamon, New York, 1986).

32. Zheng, K.; Han, X.; Wang, L.; Zhang, Y.; Yue, Y.; Qin, Y.; Zhang, X.; Zhang, Z. *Nano Lett.* **2009,** *9* (6), 2471-2476.

33. Yue, Y.; Liu, P.; Zhang, Z.; Han, X.; Ma, E. *Nano Lett.* **2011,** *11* (8), 3151-3155.

34. Wang, B.; Zhang, Z.; Chang, K.; Cui, J.; Rosenkranz, A.; Yu, J.; Lin, C.-T.; Chen, G.; Zang, K.; Luo, J. *Nano Lett.* **2018**, *18* (7), 4611-4617.

35. Vincent, L.; Djomani, D.; Fakfakh, M.; Renard, C.; Belier, B.; Bouchier, D.; Patriarche, G. *Nanotechnology* **2018**, *29* (12), 125601.

36. Liu, H.; Zheng, Z.; Yang, D.; Ke, X.; Jaatinen, E.; Zhao, J.-C.; Zhu, H. Y. *ACS Nano* **2010**, *4* (10), 6219-6227.

37. Lu, L.; Shen, Y.; Chen, X.; Qian, L.; Lu, K. *Science* **2004**, *304* (5669), 422-426.

38. Chen, Y.; Burgess, T.; An, X.; Mai, Y.-W.; Tan, H. H.; Zou, J.; Ringer, S. P.; Jagadish, C.; Liao, X. *Nano Lett.* **2016**, *16* (3), 1911-1916.

39. Chen, B.; Wang, J.; Gao, Q.; Chen, Y.; Liao, X.; Lu, C.; Tan, H. H.; Mai, Y.-W.; Zou, J.; Ringer, S. P. *Nano Lett.* **2013**, *13* (9), 4369-4373.

40. Han, X.; Zhang, Y.; Zheng, K.; Zhang, X.; Zhang, Z.; Hao, Y.; Guo, X.; Yuan, J.; Wang, Z. *Nano Lett.* **2007**, *7* (2), 452-457.